2D metal azolate framework for efficient CO_2 photoreduction

Jianxia Gu[1,3], Lingxin Wang[4], Xu Han[2,4*], Jingting He[4], Siqi You[3], Man Dong[3], Guogang Shan[3*], Danfeng He[2], Fujiang Zhou[2], Chunyi Sun[3*] and Zhongmin Su[4]

ABSTRACT Visible-light-driven conversion of CO_2 into value-added fuel is a clean and renewable technology to retard global warming and address energy shortages. Two-dimensional metal-azolate frameworks (2D MAFs) have recently received tremendous attention as CO_2 photoreduction-related catalysts due to their specific electron transport pathways, highly exposed surface-active sites, and tailorable light-absorption abilities. However, the research on 2D MAFs for efficient CO_2 photoconversion is still at the early stage. Herein, a novel 2D MAFs (compound 1) was designed by self-assembly of tetra-(4-tetrazole-phenyl)ethylene (H_4TTPE) and cobalt for CO_2 photoreduction. As a comparison, three-dimensional (3D) compound 2 was also constructed using a similar synthesis process. The experimental results of heterogeneous photocatalysis show that the photoreduction performance of 2D compound 1 is obviously better than that of 3D compound 2, exhibiting an extremely high CO production rate (11.56 mmol g^{-1} h^{-1}) in 3 h, which is 6.0-fold higher than that of compound 2 (1.94 mmol g^{-1} h^{-1}) under the same conditions. This performance advantage stems from the unique 2D structure of compound 1, which not only possesses an energy level conducive to CO_2 reduction but also facilitates efficient electron-hole separation throughout the CO_2 photoreduction process. This work paves the way for the design of 2D MAFs photocatalysts tailored for efficient CO_2 photoconversion.

Keywords: metal-azolate frameworks, two-dimensional structure, CO_2 photoreduction

INTRODUCTION

The rapid development of the global economy has led to an increase in carbon dioxide emissions, resulting in serious problems such as global warming and the energy crisis [1,2]. Therefore, it is urgent to develop environmentally friendly solutions to address these issues. Inspired by the photosynthesis in nature, the plausible photocatalytic reduction of CO_2 to reusable hydrocarbons (such as CO, CH_4, C_2H_5OH, and CH_3 OH) offers an alternative opportunity for global sustainable energy development [3,4]. Among the target products, CO is widely favored due to its simple separation, easy synthesis of

liquid fuels *via* Fischer-Tropsch, and low resistance in the reduction process [5]. To date, many endeavour have been engaged in developing high-efficiency photocatalysts for CO_2 photoreduction to CO [6,7]. Noble metals have been extensively used as photocatalysts for some fundamental catalytic reactions for their high CO_2 reduction performance to CO [8,9]. Still, they are not suitable for commercial use owing to their high price, high toxicity, and poor durability. Consequently, rational design of highly efficient and durable photocatalysts remains crucial and challenging for achieving high "solar-CO" capability.

Metal-organic frameworks (MOFs) have shown superior properties, such as tailorable composition and structures, tunable pores, as well as modifiable surface properties, which make them obtain spacious application prospects in the fields of catalysis, gas adsorption and separation [10–12]. As a subclass of MOFs, metal-azolate frameworks (MAFs) have recently emerged as hybrid material that can form one-dimensional (1D), two-dimensional (2D), and three-dimensional (3D) extended structures through self-assembly polyazole ligand (such as imidazole, triazole, and tetrazole) and metal ions [13,14]. It is well known that 2D MAFs have received increasing attention owing to their superior characteristics of high aspect ratio, large surface area, abundant exposed active sites, and adjustable chemical compositions [15]. These superior advantages render 2D MAFs outstanding from 3D materials for photocatalysis application because of: i) 2D MAFs' suitable band structures that trigger the rapid separation of light-induced electrons and holes, ii) the massive active sites to enhance the contact between the catalyst surface and molecules as well as promote the surface redox reactions in photocatalysis, iii) minimizing the pathways associated with electron transport [16–18]. Hence, 2D MAFs offer great opportunities to overcome challenges encountered in CO_2 photoreduction. However, they have been less studied for photocatalytic reduction of CO_2.

In this work, a novel model MAF, $[Co_2(H_2O)_5(H_4TTPE)_{0.5}]\cdot$ H_2O (denoted as **compound 1**) was synthesized through a solvothermal synthesis method as photocatalysts for CO_2 reduction. And the single-crystal X-ray diffraction (XRD) confirms that **compound 1** features a 2D structure based on a tetranuclear cobalt cluster. Simultaneously, another MAF **compound 2** was designed, with a 3D structure composed of tetra-(4-tetrazole-phenyl)ethylene (H_4TTPE) and Co–O chains as building blocks,

[1] Department of Chemistry, Xinzhou Normal University, Xinzhou 034000, China
[2] College of Science, Qiongtai Normal University, Haikou 571100, China
[3] National & Local United Engineering Laboratory for Power Batteries, Key Laboratory of Polyoxometalate Science of Ministry of Education, Department of Chemistry, Northeast Normal University, Changchun 130024, China
[4] School of Chemical and Environmental Engineering, Changchun University of Science and Technology, Changchun 130022, China
* Corresponding authors (emails: 2018200108@mails.cust.edu.cn (Han X); Shangg187@nenu.edu.cn (Shan G); Suncy009@nenu.edu.cn (Sun C))

to serve as a contrasting material. In this study, H_4TTPE was chosen to been as ligand for the following considerations [18,19]: a) metal-nitrogen (M–N) bonds often endow excellent thermal and chemical stability to the host frameworks, b) the overlap between the π-orbitals of conjugated azolate ligands and the d-orbitals of metal ions achieves efficient delivery of the charge transfer, c) there are abundant N atom sites on the surface of the framework prepared by polyazole, which functionalize the surface of pores to improve the affinity of guests. The synthesized framework acted as a photocatalyst under simulated solar light ($\lambda \geq 420$ nm) for CO_2 conversion. Under the same condition, 2D **compound 1** presents an 11.56 mmol g^{-1} h^{-1} CO evolution rate for 3 h, about 6.0-fold that of 3D **compound 2** (1.94 mmol g^{-1} h^{-1}). The exceptional photoreduction performance of **compound 1** can be attributed primarily to its unique 2D structure, as evidenced by the following factors: (1) Ultraviolet (UV) testing and Mott-Schottky calculations demonstrate that the 2D structure possesses an appropriate bandgap facilitating CO_2 reduction. (2) Results from transient photocurrent measurements suggest that the 2D structure promotes efficient electron-hole separation. Consequently, 2D **compound 1** holds considerable potential for applications in environmental purification and related domains.

EXPERIMENTAL SECTION

Materials and reagents

$CoCl_2 \cdot 6H_2O$, $[Ru(bpy)_3]Cl_2 \cdot 6H_2O$ were purchased from Alfa, and H_4TTPE for the synthesis was purchased from Tensus Biotech(Shanghai) Co. The purity of all reagents was of analytical grade. They were used without further purification. Deionized water was used in all the experiments.

Sample preparation

*Synthesis of $[Co_2(H_2O)_5(H_4TTPE)]\cdot(H_4TTPE)_{0.5}\cdot H_2O$ (**compound 1**)*
Compound 1 was synthesized *via* the solvothermal reactions. $CoCl_2 \cdot 6H_2O$ (0.25 mmol, 0.0685 g), H_4TTPE (0.1 mmol,

0.0601 g), deionized water (45 mL), and acetonitrile (5 mL) were sealed in a 100-mL Teflon-lined stainless-steel vessel. Then the mixture was heated at 120°C for 84 h and gradually cooled to room temperature. The obtained orange block crystals were washed three times with deionized water and dried in air (Yield: 87% based on H_4TTPE). $C_{45}H_{38}Co_2N_{24}O_6$, crystal system: triclinic, space group: P$\bar{1}$.

*Synthesis of $[Co_2(H_2O)_3(H_4TTPE)_{0.5}]$ (**compound 2**)*
Compound 2 was synthesized using the same stoichiometric ratio as **compound 1**. Briefly, $CoCl_2 \cdot 6H_2O$ (0.25 mmol, 0.0685 g) and H_4TTPE (0.1 mmol, 0.0601 g) were dissolved in *N,N*-dimethylformamide (DMF, 20 mL), deionized water (5 mL), and $NH_3 \cdot H_2O$ (3 mL). Then the mixture was sealed in a Parr Teflon-lined stainless-steel vessel and heated at 130°C for three days. After gradually cooling to room temperature, salmon fusiformis crystals were obtained, washed with DMF and dried in air (Yield: 79%, based on H_4TTPE). $C_{30}H_{16}Co_3N_{16}O_6$, crystal system: monoclinic, space group: C2/*m*

RESULTS AND DISCUSSION

Crystal structures

The structure of **compound 1** was determined by single-crystal XRD and the results are shown in Fig. 1. Orange crystals are synthesized through the solvothermal reaction of cobalt chloride and H_4TTPE in water and acetonitrile at 120°C for 84 h. Complex crystallizes in the triclinic system space group P$\bar{1}$ and displays a highly complicated 2D polymeric network as summarized in Table S1. Its asymmetric unit contains two Co (II) ions, one H_4TTPE ligand, and a half water molecule (Fig. S1a). There are two crystallographically independent Co (II) ions exhibiting six-connected octahedral coordination geometries. Although both Co1 and Co2 atoms have distorted octahedral coordination geometry, their coordination environments are different. Each Co1 ion is octahedrally coordinated by four N-atoms derived from four bridging H_4TTPE-fragments, and two O-atoms from two water molecules, while Co2 is six coordinated
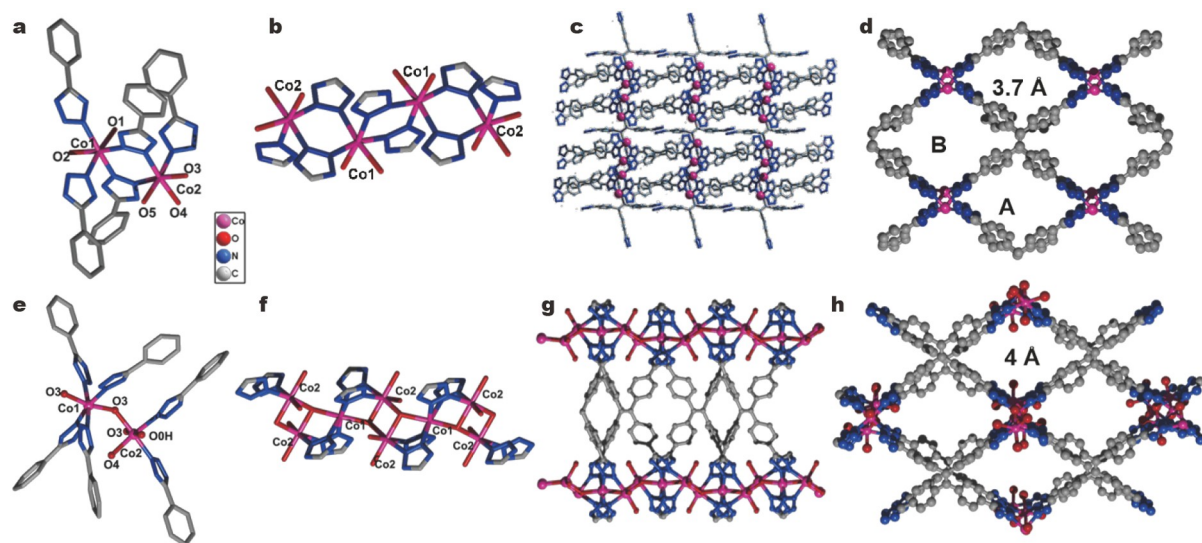

Figure 1 Schematic of the crystal structures of **compound 1** and **compound 2**. (a, e) The view of coordination environment of Co (II) in **compound 1** and **compound 2**. (b, f) The arrangement phalanx of the ligands with Cobalt cluster in **compound 1** and **compound 2**. (c, g) The neatly organized 2D layer with Cobalt cluster as nodes for **compound 1** and **compound 2**. (d, h) The windows in **compound 1** and **compound 2**. The coordinated H atoms are omitted for clarity (color modes: Co, hot pink; N, blue; O red; C gray-25%).

in an octahedral coordination geometry defined by three O-atoms from three water molecules and three N-atoms from three bridging H_4TTPE-fragments, as depicted in Fig. 1a. In addition, each H_4TTPE ligand connects seven cobalt atoms by adopting a $\mu_2:\eta_1:\eta_1$ coordination mode of three binuclear cobalt secondary building units (SBUs) and one mononuclear cobalt SBU, as revealed in Fig. S1b, respectively. The Co2, Co1, Co1, and Co2 are connected with eight tetrazolyl groups into a four-nuclear {Co4} cluster with Co/Co distances of 3.448 and 3.526 Å as illustrated in Fig. 1b and Table S2, which are further by a bridge of water molecules to form 1D metal ladders. The 1D metal ladders propped up the next 1D metal ladders by free ligands to produce a 2D framework. According to single-crystal data of **compound 1**, free ligands only exist as guest molecules in type B pores (Fig. S1b). The diagonal tetrazolium ring of the free guest molecules is inserted into the type of B pore vertically on the next layer (Fig. S1c, S1d). The resulting sandwich structure contains a layer of guest molecules between layers of host molecules, as shown in Fig. 1c. The resulting network comprises a rhombic channel with a pore aperture size of 3.7 Å named A along the crystallographic c-axis (Fig. 1d).

The single-crystal XRD analysis reveals that **compound 2** crystallizes in the monoclinic space group $C2/m$ and displays a highly complicated 3D neutral framework. As shown in Fig. 1e, each Co1 is six-coordinated by two oxygen atoms from two water molecules (Co1–O 2.126 (2)-2.126 (2) Å), and four N-atoms derive from four bridging H_4TTPE-fragments (Co1–N 2.122 (4)-2.129(3) Å). Each Co2 atom is six-coordinated by three oxygen atoms from three water molecules (Co2–O 2.095 (3)-2.123 (3) Å), and two N-atoms derive from two H_4TTPE ligands (Co–N 2.131 (4)-2.152 (3) Å). Mononuclear Co1 and binuclear Co2 cluster are coordinated by μ_3-O to form a trinuclear {Co$_3$O$_6$} cluster with Co–Co distance of 3.396 and 3.911 Å (Table S3). The {Co$_3$O$_6$} clusters, as rod-shaped secondary building units, are further linked to neighboring {Co$_3$O$_6$} clusters to form a 1D metal ladder (Fig. 1f, g). Then, these 1D chains are further connected by H_4TTPE ligands to assemble a 3D open framework with rhombic channels of 4 Å in diameter along the crystallographic a-axis (Fig. 1h and Fig. S2).

Characterization of materials

The phase purity and crystal structure of **compound 1** and **compound 2** were confirmed using powder XRD patterns (PXRD) (Fig. 2a and Fig. S3). The characteristic diffraction peaks of **compound 1** and **compound 2** are well-matched with the simulation, indicating the high phase purity of the compounds. The morphology of **compound 1** was characterized by scanning electron microscope (SEM), and the Fig. S4 clearly shows the detail morphology of **compound 1** under different magnifications. The CO_2 adsorption-desorption curves of **compound 1** were also obtained to investigate its CO_2 adsorption property (Fig. S5). It is found that **compound 1** possesses the ability to adsorb CO_2, which is beneficial for CO_2 photoreduction. In addition, Fourier Transform infrared spectroscopy (FT-IR) analysis was employed to determine the chemical bonds and functional groups of photocatalysts. The FT-IR spectrum of **compound 1** sample is depicted in Fig. 2b, the wide signal at 3386 cm^{-1} is assigned to O–H vibration, testifying the presence
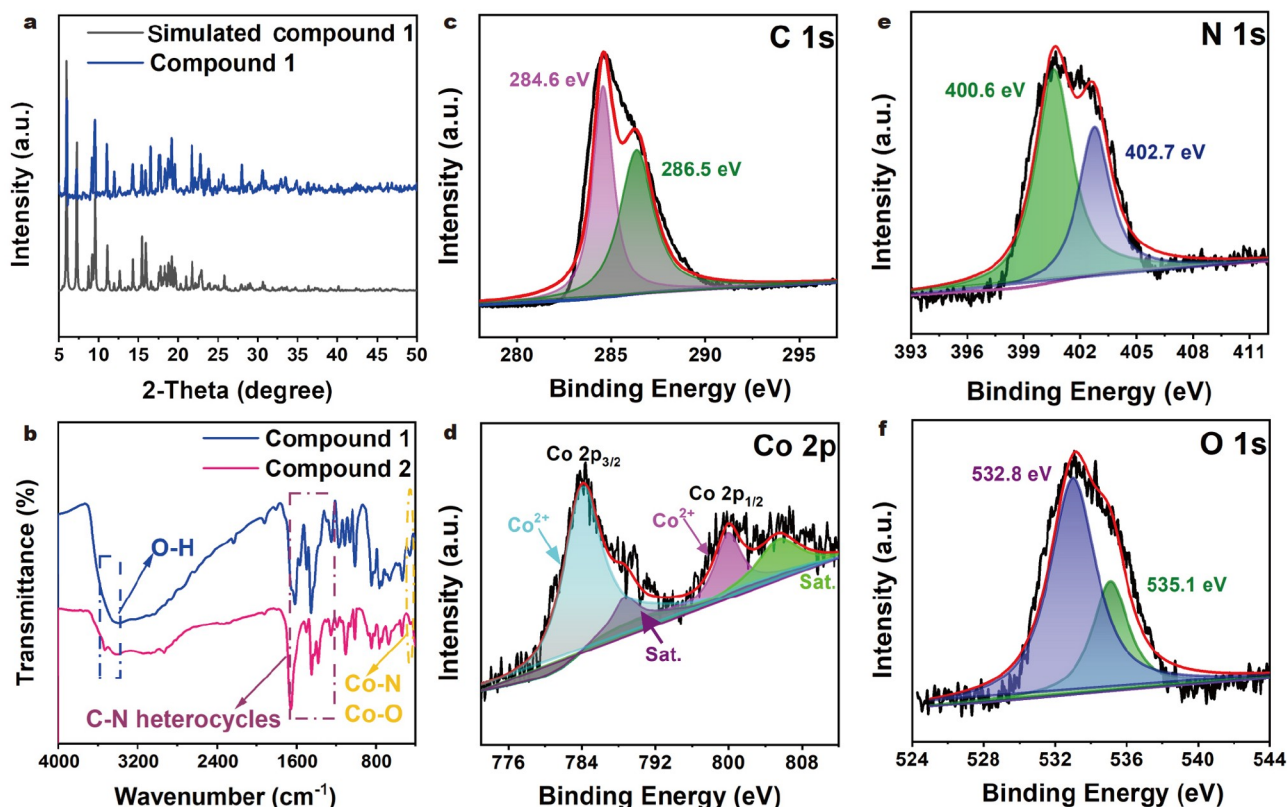

Figure 2 (a) PXRD profiles as made with that simulated obtained from single-crystal XRD for **compound 1**. (b) FT-IR spectra showing characteristic selective peaks of **compound 1** (blue) and **compound 2** (rose) referenced to KBr, respectively. High-resolution XPS spectra of **compound 1** of (c) C 1s, (d) Co 2p, (e) N 1s, and (f) O 1s.

of free water in all the prepared samples [20]. Another broad peak at around 3195 cm^{-1} is attributed to the stretching mode of the N–H group in H$_4$TTPE at the defect sites of the aromatic ring [21,22]. The peaks from 1200 to 1616 cm^{-1} belong to the typical stretching vibrations of C–N in the heterocycles [23]. The intense symmetric Co–N stretching vibration at around 455 cm^{-1} provides evidence to confirm the metal-ligand bond [24,25]. For the FT-IR spectrum of **compound 2**, the wide signal at 3398 cm^{-1} is assignable to O–H vibration, testifying that the water molecules exist in all the prepared samples. The peak at 2928 cm^{-1} is attributed to the C–H bond. The prominent peak located at about 448 cm^{-1} is assigned to the stretching vibration of the Co–O bond [24]. Thermo-gravimetric analysis (TGA) is executed to investigate the thermal stability of **compound 1** and **compound 2** (Fig. S6) at 25–800°C under an N$_2$ atmosphere, revealing that they remain stable up to approximately 240 and 220°C, respectively [25]. The full survey spectrum of X-ray photoelectron spectroscopy (XPS) indicates that **compound 1** (Fig. S7a) and **compound 2** (Fig. S7b) are composed of C, N, Co, and O. XPS measurements were carried out to explore the chemical statuses and environments of the elements in **compound 1**, which were displayed in Fig. 2. From the XPS spectrum of **compound 1**, the C 1s spectrum can be deconvoluted into two peaks centered at 284.6 and 286.5 eV (Fig. 2c) [26]. These signals correspond to the benzene ring and C–N in the

H$_4$TTPE ligand, respectively. Meanwhile, the high-resolution spectrum of Co 2p reveals two typical peaks located at 784.1 and 800.1 eV, with the separation of 15.8 eV. This result is consistent with the previous reports and can be ascribed to the Co 2p3/2 and Co 2p1/2 spin-orbit peaks, respectively. Both Co 2p3/2 and Co 2p1/2 peaks show their corresponding firm satellite peaks at 788.0 and 805.6 eV (Fig. 2d). These findings suggest that the oxidation state of Co in the MAFs is +2 [27,28]. As depicted in Fig. 2e, the N 1s spectrum presentes two deconvoluted peaks at 400.6 and 402.7 eV, ascertaining sp2 hybridized N atoms in graphitic N and nitrogen oxides, respectively [29]. Additionally, the O 1s spectrum (Fig. 2f) can be divided into two peaks at 532.8 and 535.1 eV. The peak at 532.8 eV is attributed to the N–Co–O, implying the synthesis of **compound 1**. The peak observed at 535.1 eV results from a small amount of physically adsorbed water molecules [30]. The XPS analysis of **compound 2** is shown in Fig. S7c–f, wherein the high-resolution spectrum of Co 2p suggests that the central metal ion in **compound 2** is in a divalent state (Fig. S7d).

Photocatalytic CO$_2$ reduction performance

The photocatalytic performance of **compound 1** and **compound 2** for CO$_2$ reduction is evaluated under the optimized reaction as shown in Fig. 3 and Fig. S10. All the photocatalytic reductions were performed under moderate conditions in a CO$_2$-saturated
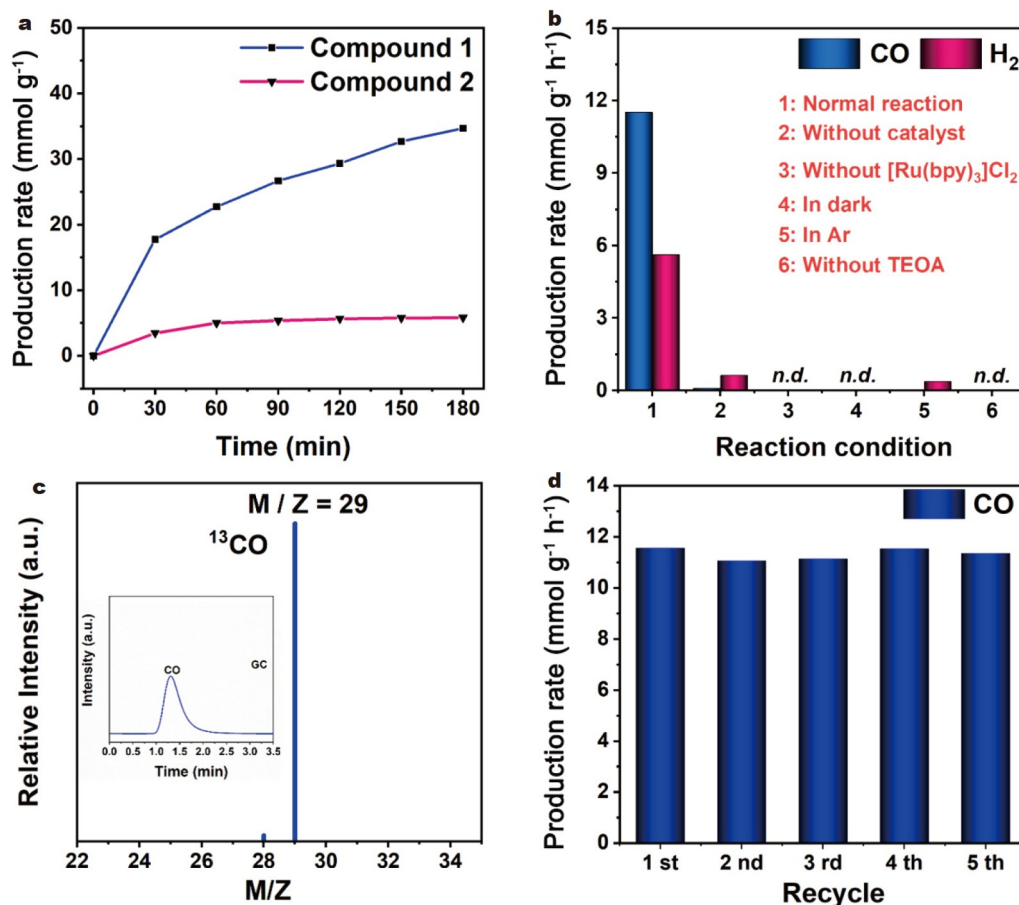

Figure 3 (a) CO evolution for the visible-light irradiated photocatalytic system with **compound 1** and **compound 2** within 3 h. (b) Products of photocatalytic-control system under various reaction conditions. Including using only [Ru(bpy)$_3$]Cl$_2$, replacing CO$_2$ with Ar, without [Ru(bpy)$_3$]Cl$_2$, light, or TEOA ("n.d." means "not detectable"). (c) Mass spectrum of ^{13}CO produced from the photocatalytic reduction for ^{13}CO$_2$ with **compound 1**. (d) Stability tests of **compound 1** photocatalyst with 3 h for each run.

atmosphere at 25°C with the assistance of $[Ru(bpy)_3]Cl_2 \cdot 6H_2O$ (a photosensitizer) under visible light ($\lambda \geq 420$ nm). The solvent system (50 mL), consisting of triethanolamine (TEOA):CH_3CN: CH_3OH in a 1:3:2 ratio, employs MeOH as the proton donor [31,32], while TEOA serves as the sacrificial agent [33]. Notably, only CO and H_2 are produced as gaseous products without the presence of other hydrocarbon species. In other words, CO_2 is exclusively reduced to CO in this photocatalytic process, with H_2O being transformed into H_2 as the only by-product. **Compound 1** shows notable photocatalytic activity for CO_2 reduction and the amounts of CO and H_2 generated increase steadily with the illumination time at different reaction rates. The average CO evolution attains 20.52 mmol g^{-1} h^{-1} in 1 h of reaction with a selectivity of 65.5% over competing for H_2 generation, where the H_2 evolution is 10.83 mmol g^{-1} h^{-1} (Fig. S8). Within 3 h, the CO yield of **compound 1** reaches 11.56 mmol g^{-1} h^{-1} (Fig. 3a). In contrast, **compound 2** shows lower CO productions of 4.37 and 1.94 mmol g^{-1} h^{-1} in 1 h and 3 h, respectively (Fig. 3a and Fig. S10a). **Compound 1** in photocatalytic test systems can transform CO_2 into CO and its formation rate is comparable to, or even higher than, that of highly active Co-based semiconductors (Table S4). To further confirm the photocatalytic activity of **compound 1**, a series of control tests were performed and demonstrated in Fig. 3b. Firstly, the production rate of CO is dramatically reduced when the $[Ru(bpy)_3]Cl_2 \cdot 6H_2O$ is used alone (**compound 1** catalyst is absent), highlighting the significant role of the catalyst in the reaction. Meanwhile, Ar was introduced into the reduction system, instead of CO_2, during the photocatalytic test with **compound 1** as the catalyst. Merely a small amount of H_2 gas is produced without any detectable CO, implying that produced CO comes from the reduction of CO_2 in the conventional experiment rather than surface carbonaceous residuals of photocatalysts. Furthermore, no gaseous product (CO or H_2) is detected by gas chromatography (GC) in the absence of $[Ru(bpy)_3]Cl_2 \cdot 6H_2O$, visible light irradiation or TEOA. These results illustrate the indispensability of the photosensitizer, sacrificial agent, and illumination in the process of CO_2 photoreduction using **compound 1**. A series of control tests of **compound 2** were performed and demonstrated in Fig. S10b, with the conclusion being consistent with that of **compound 1**. Additionally, the photocatalytic activity of the ligand H_4TTPE in the **compound 1** was studied under the same catalytic environment (Fig. S9). After 1 h, the free H_4TTPE ligand has less effect on the photocatalytic reduction of CO_2 compared to **compound 1**, which indicates that the interference of the H_4TTPE free ligand in **compound 1** is also excluded. The apparent quantum efficiency (AQE) for CO evolution on **compound 1** is determined to be 1.26% at 420 nm monochromatic light, based on the formula in the Supplementary information. This value is higher than that of many other reported photocatalysts (Table S5).

To provide an unambiguous evidence for the carbon source of the evolved CO, ^{13}C-isotopic tracer experiments were carried out under identical reaction conditions. The resulting data, as shown in Fig. 3c and Fig. S10c, reveal that the peak at m/z = 29 corresponds to ^{13}CO [34,35], strongly indicating that the generated CO arises from the photocatalytic reduction of CO_2 molecules rather than from an organic solvent, decomposition of **compound 1**, **compound 2** or the photosensitizer itself. Photocatalytic stability of **compound 1** and **compound 2** were explored through cycling experiments. Additionally, photo-

catalytic stability was explored through cycling experiments of **compound 1** and **compound 2**, as depicted in Fig. 3d and Fig. S10d. The recycling experiment demonstrates that the catalytic system could maintain at least five cycles, and the crystallinity and structural integrity of **compound 1** and **compound 2** are retained after the reaction, as confirmed by PXRD characterizations in Fig. S11. These results confirm that the novel 2D **compound 1** is an efficient, recycled, and stable heterogeneous photocatalyst for CO_2 photoreduction.

Possible photocatalytic mechanism

An *in situ* infrared spectrum analysis was performed on **compound 1** to identify the reaction intermediates during the CO_2 photoreaction process. Experimental data were collected and analyzed at different time intervals. The characteristic peaks observed at 1352, 1508, and 1623 cm^{-1} (Fig. 4a) are attributed to COOH*, a crucial intermediate in the conversion of CO_2 to CO. Furthermore, the intensity of the COOH* peaks steadily increases with prolonged light irradiation, suggesting that CO_2 is continuously converted into CO [36,37].

Understanding the mechanism of photocatalytic reactions involves comprehending the band matching and transfer routes of photo-generated carriers. Firstly, the optical properties of **compound 1** and **compound 2** were examined by ultraviolet-visible (UV-vis) spectroscopy (Fig. 4b) [38]. The band gaps (E_g) of **compound 1** and **compound 2** are estimated to be 2.30 and 2.72 eV from the Tauc plot, respectively (see the insert of Fig. 4b), unveiling their potential as semiconducting photocatalysts. Moreover, the Mott-Schottky (M-S) curve is used to gain the ionization potential which is equal to the flat-band potential, and the flat-band potential of **compound 1** is -1.07 eV *versus* Ag/AgCl (≈ -0.87 eV *vs.* NHE). Meanwhile, the M-S plot shows that the slope of the tangent line of **compound 1** is positive, indicating that **compound 1** is an n-type semiconductor. It is known that the conduction band (CB) of the n-type semiconductor is about 0.1 eV negative to the flat-band potential [39,40]. Accordingly, the CB is assigned to -0.97 eV *versus* NHE for **compound 1** (Fig. 4c). The valence bands (VB) of **compound 1** is calculated to be 1.33 eV (*vs.* NHE) according to the equation ($E_{CB} = E_{VB} - E_g$). Additionally, the values of E_{CB} (-0.86 eV) and E_{VB} (1.86 eV) for **compound 2** are obtained according to the same calculation method (Fig. S12a). The energy level structures indicate that the photo-generated electrons can migrate to the CO_2 molecule for reduction on the **compound 1** and **compound 2** ($CO_2/CO = -0.53$ *vs.* NHE, $H^+/H_2 = -0.42$ *vs.* NHE) [5]. Notably, **compound 1** exhibits a larger energy level difference with the reduction products than **compound 2**, potentially favoring the occurrence of a reduction reaction and enhancing catalytic activity. This advantage of **compound 1** is attributed to its unique 2D structure, which confers a suitable band gap.

To gain deeper insight into the electron transfer process during CO_2 photoreduction on 2D **compound 1**, a luminescent quenching experiment was conducted by introducing **compound 1** and TEOA into a CH_3CN solution containing $[Ru(bpy)_3]Cl_2$. As shown in Fig. S13, the CH_3CN solution of $[Ru(bpy)_3]Cl_2$ exhibits an emission band centered at 622 nm at an excitation wavelength of 460 nm [41,42]. The addition of TEOA results in minimal change in the photoluminescence intensity of $[Ru(bpy)_3]^{2+}$ (Fig. S13a), while introducing varying amounts of **compound 1** into the CH_3CN solution of
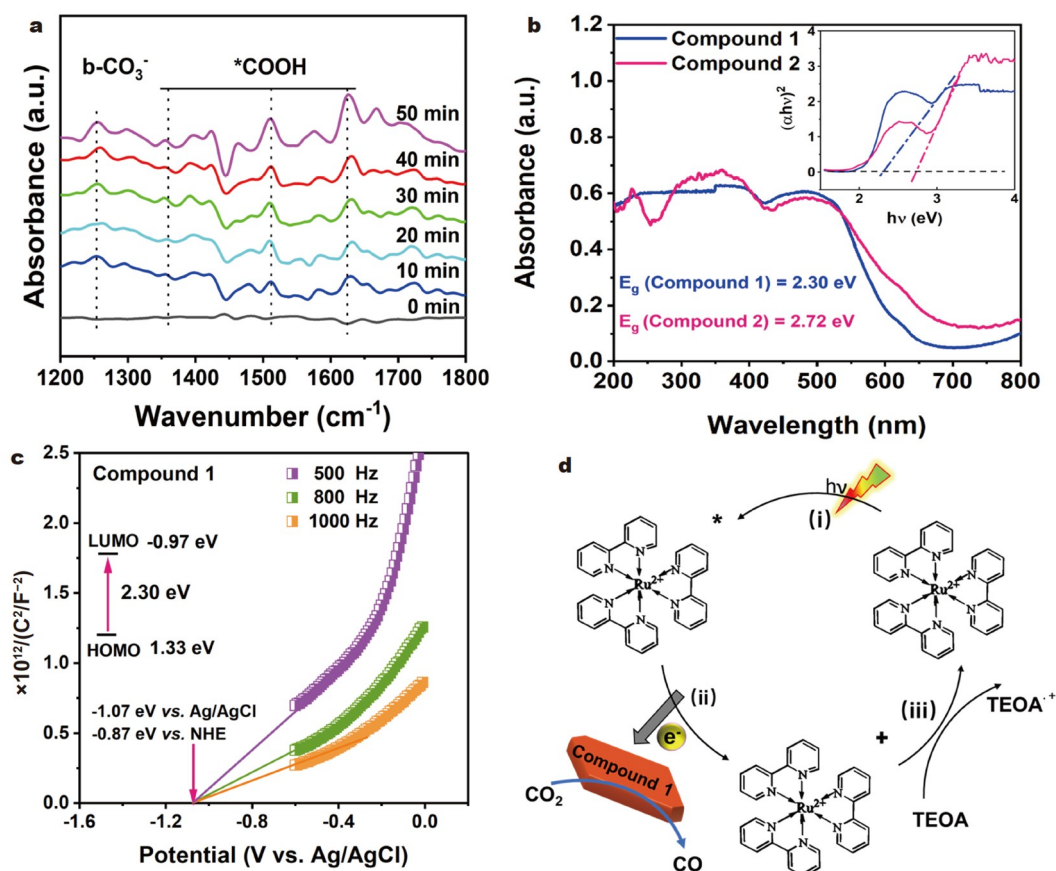
Figure 4　(a) *In situ* infrared spectra of CO_2 photoreduction on **compound 1** with a cut-off 420-nm filter under simulated sunlight irradiation. (b) UV-Vis spectra of **compound 1** and **compound 2**, inset is Tauc plots of $(\alpha h\nu)^2$ *vs.* energy ($h\nu$) for the band gap energy of **compound 1** and **compound 2**. (c) The *M-S* curves of **compound 1** under different frequencies, inset is the energy diagram of the HOMO and LUMO levels of **compound 1**. (d) The agency of photocatalytic CO_2 reduction in such a photocatalytic system.

$[Ru(bpy)_3]Cl_2$ leads to noticeable photoluminescence quenching (Fig. S13b). These experimental results indicate that excited electrons transfer from the photosensitizer ($[Ru(bpy)_3]Cl_2$) to **compound 1**, rather than to TEOA [43]. The separation of electrons and holes plays a crucial role in photocatalysis. To investigate the charge separation efficiency of **compound 1** and **compound 2**, transient photocurrent tests were conducted in the same electrolyte under a 20-s light-on/off cycle at 0.3 V (*vs.* SCE). As depicted in Fig. S14, both catalysts exhibit rapid increase and decay of photocurrent values upon illumination and turning off the light, respectively, indicating their good responsiveness to light. Remarkably, **compound 1** exhibits a current density of 10 $\mu A\ cm^{-2}$, which is 50% higher than that of **compound 2**. The differences in charge separation between **compound 1** and **compound 2** are likely due to their structural disparities, resulting in differing activities for photocatalytic CO_2 reduction reaction (CO_2RR).

Drawing upon the preceding results, a reaction mechanism was proposed accompanied by energy-level diagrams to elucidate the electron-hole transfer dynamics throughout the photocatalytic process, including the electrons transfer from $[Ru(bpy)_3]Cl_2·6H_2O$ to **compound 1** (Fig. S15) [44]. The lowest unoccupied molecular orbital (LUMO) and the highest occupied molecular orbital (HOMO) energy levels of $[Ru(bpy)_3]Cl_2·6H_2O$ are −1.25 and 1.24 eV respectively, *versus* NHE [45]. Upon

photoexcitation, both **compound 1** and $[Ru(bpy)_3]Cl_2·6H_2O$ produce the electron-hole pairs, the CB of **compound 1** (−0.97 eV *vs.* NHE) is lower than that of $E(Ru(bpy)_3^{2+*}/Ru(bpy)_3^{+})$, causing the photoexcited electrons of $[Ru(bpy)_3]Cl_2·6H_2O$ to migrate to the CB of **compound 1** and effectively inhibit the photoelectron-hole recombination of $[Ru(bpy)_3]Cl_2·6H_2O$, thereby, implementing CO_2 photoreduction. In heterogeneous photocatalytic systems, $[Ru(bpy)_3]Cl_2$, upon irradiation, remains in an excited state. Electrons from this excited state ($[Ru(bpy)_3]^{2+*}$) transfer to the photocatalyst **compound 1**, where CO_2 is activated and reduced to CO. Simultaneously, **compound 1** oxidatively quenches $[Ru(bpy)_3]^{2+*}$, yielding the reduced species $[Ru(bpy)_3]^{+}$. Ultimately, sacrificial electron donor TEOA oxidizes $[Ru(bpy)_3]^{+}$ back to $[Ru(bpy)_3]^{2+}$, completing the entire catalytic cycle (Fig. 4d) [46]. The electron-hole transfer process involved in CO_2 photoreduction on **compound 2** is analogous to that observed with **compound 1**, and a corresponding energy-level diagram is presented in Fig. S12b.

CONCLUSIONS

In summary, two novel MAFs (2D **compound 1** and 3D **compound 2**) based on tetrazole are designed and synthesized to be outstanding visible light photocatalysts for CO_2 reduction. **Compound 1**, characterized by its unique 2D structure, exhibits significantly ~6-fold higher photocatalytic CO production

$(11.56 \text{ mmol g}^{-1}\text{ h}^{-1})$ than **compound 2** $(1.94 \text{ mmol g}^{-1}\text{ h}^{-1})$. Furthermore, **compound 1** demonstrates excellent recyclability under experimental conditions. Photocurrent tests and M-S plots reveal that **compound 1** possesses superior electron-hole separation and an energy level structure more favorable for CO_2 reduction than **compound 2**. Given that the rationally designed crystalline MAFs system incorporates tetrazole components, our findings are expected to pave the way for the development of tetrazole-based MAFs for applications in artificial photosynthesis.

1 Li X, Yu J, Jaroniec M, *et al.* Cocatalysts for selective photoreduction of CO_2 into solar fuels. Chem Rev, 2019, 119: 3962–4179

2 Gu J, Chen W, Shan GG, *et al.* The roles of polyoxometalates in photocatalytic reduction of carbon dioxide. Mater Today Energy, 2021, 21: 100760

3 Wang YJ, Wang HJ, Luo F, *et al.* Inter-clusters synergy in iron-organic frameworks for efficient CO_2 photoreduction. Appl Catal B-Environ, 2022, 300: 120487

4 Zhang M, Zhang D, Jing X, *et al.* Engineering NH_2-Cu-NH_2 triple-atom sites in defective MOFs for selective overall photoreduction of CO_2 into CH_3COCH_3. Angew Chem Int Ed, 2024, 63: e202402755

5 Zhang H-, Hong Q-, Li J, *et al.* Isolated square-planar copper center in boron imidazolate nanocages for photocatalytic reduction of CO_2 to CO. Angew Chem Int Ed, 2019, 58: 11752–11756

6 Wang J, Lin S, Tian N, *et al.* Nanostructured metal sulfides: classification, modification strategy, and solar-driven CO_2 reduction application. Adv Funct Mater, 2021, 31: 2008008

7 Gao C, Wang J, Xu H, *et al.* Coordination chemistry in the design of heterogeneous photocatalysts. Chem Soc Rev, 2017, 46: 2799–2823

8 Hao M, Qiu M, Yang H, *et al.* Recent advances on preparation and environmental applications of MOF-derived carbons in catalysis. Sci Total Environ, 2021, 760: 143333

9 Peng Y, Kang S, Hu Z. Pt nanoparticle-decorated CdS photocatalysts for CO_2 reduction and H_2 evolution. ACS Appl Nano Mater, 2020, 3: 8632–8639

10 Gu JX, Zhao X, Sun Y, *et al.* A photo-activated process cascaded electrocatalysis for the highly efficient CO_2 reduction over a core-shell ZIF-8@Co/C. J Mater Chem A, 2020, 8: 16616–16623

11 Du C, Zhang Z, Yu G, *et al.* A review of metal organic framework (MOFs)-based materials for antibiotics removal *via* adsorption and photocatalysis. Chemosphere, 2021, 272: 129501

12 Ding M, Cai X, Jiang HL. Improving MOF stability: approaches and applications. Chem Sci, 2019, 10: 10209–10230

13 Aubrey ML, Wiers BM, Andrews SC, *et al.* Electron delocalization and charge mobility as a function of reduction in a metal-organic framework. Nat Mater, 2018, 17: 625–632

14 Zhang JP, Zhang YB, Lin JB, *et al.* Metal azolate frameworks: from crystal engineering to functional materials. Chem Rev, 2012, 112: 1001–1033

15 Han X, He X, Wang F, *et al.* Engineering an N-doped Cu_2O@N–C interface with long-lived photo-generated carriers for efficient photoredox catalysts. J Mater Chem A, 2017, 5: 10220–10226

16 Yang K, Li J, Zhou L, *et al.* Synthetic strategies of two-dimensional porous materials towards highly effective catalysts. FlatChem, 2019, 15: 100109

17 He T, Ni B, Zhang S, *et al.* Ultrathin 2D zirconium metal-organic framework nanosheets: preparation and application in photocatalysis. Small, 2018, 14: e1703929

18 Li SL, Lan YQ, Qin JS, *et al.* Assembly of 3D metal-organic frameworks based on different helical units: chiral and achiral structures constructed by length-modulated N-donor ligands. Cryst Growth Des, 2009, 9: 4142–4146

19 Lan A, Li K, Wu H, *et al.* A luminescent microporous metal-organic framework for the fast and reversible detection of high explosives. Angew Chem Int Ed, 2009, 48: 2334–2338

20 Shi H, He X. Large-scale synthesis and magnetic properties of cubic CoO nanoparticles. J Phys Chem Solids, 2012, 73: 646–650

21 Gu P, Wu H, Jing T, *et al.* (4,5,8)-connected cationic coordination polymer material as explosive chemosensor based on the *in situ* generated AIE tetrazolyl-tetraphenylethylene derivative. Inorg Chem, 2021, 60: 13359–13365

22 Shi W, Guo F, Chen J, *et al.* Hydrothermal synthesis of $InVO_4$/Graphitic carbon nitride heterojunctions and excellent visible-light-driven photocatalytic performance for rhodamine B. J Alloys Compd, 2014, 612: 143–148

23 Guo F, Shi W, Zhu C, *et al.* CoO and g-C_3N_4 complement each other for highly efficient overall water splitting under visible light. Appl Catal B-Environ, 2018, 226: 412–420

24 Zhong M, Liang B, Fang D, *et al.* Leaf-like carbon frameworks dotted with carbon nanotubes and cobalt nanoparticles as robust catalyst for oxygen reduction in microbial fuel cell. J Power Sources, 2021, 482: 229042

25 Cui D, Bai F, Zhang L, *et al.* Piezofluorochromism in hierarchical porous π-stacked supermolecular spring frameworks from aromatic chiral cages. Angew Chem Int Ed, 2024, 63: e202319815

26 Xue Y, Lu S, Liang Z, *et al.* Porous graphitic carbon nitride with nitrogen defects and cobalt-nitrogen (Co N) bonds for efficient broad spectrum (visible and near-infrared) photocatalytic H_2 production. J Colloid Interface Sci, 2020, 561: 719–729

27 Huang Q, Guo Y, Wang X, *et al.* In-MOF-derived ultrathin heteroatom-doped carbon nanosheets for improving oxygen reduction. Nanoscale, 2020, 12: 10019–10025

28 Adeel M, Canzonieri V, Daniele S, *et al.* 2D metal azolate framework as nanozyme for amperometric detection of glucose at physiological pH and alkaline medium. Microchim Acta, 2021, 188: 77

29 Wang L, Jin P, Huang J, *et al.* Integration of copper(II)-porphyrin zirconium metal-organic framework and titanium dioxide to construct Z-scheme system for highly improved photocatalytic CO_2 reduction. ACS Sustain Chem Eng, 2019, 7: 15660–15670

30 Chen Q, Li S, Xu H, *et al.* Co-MOF as an electron donor for promoting visible-light photoactivities of g-C_3N_4 nanosheets for CO_2 reduction. Chin J Catal, 2020, 41: 514–523

31 Ye L, Gao Y, Cao S, *et al.* Assembly of highly efficient photocatalytic CO_2 conversion systems with ultrathin two-dimensional metal-organic framework nanosheets. Appl Catal B-Environ, 2018, 227: 54–60

32 Wang J, Cherevan AS, Hannecart C, *et al.* Ti-based MOFs: New insights on the impact of ligand composition and hole scavengers on stability, charge separation and photocatalytic hydrogen evolution. Appl Catal B-Environ, 2021, 283: 119626

33 Cao Y, Chen S, Luo Q, *et al.* Atomic-level insight into optimizing the hydrogen evolution pathway over a Co_1-N_4 single-site photocatalyst. Angew Chem Int Ed, 2017, 56: 12191–12196

34 Dong H, Zhang X, Lu Y, *et al.* Regulation of metal ions in smart metal-cluster nodes of metal-organic frameworks with open metal sites for improved photocatalytic CO_2 reduction reaction. Appl Catal B-Environ, 2020, 276: 119173

35 Bie C, Zhu B, Xu F, *et al. In situ* grown monolayer N-doped graphene on CdS hollow spheres with seamless contact for photocatalytic CO_2 reduction. Adv Mater, 2019, 31: e1902868

36 You SQ, Dong YJ, Hou BS, *et al.* $[W_{10}O_{32}]^{4-}$-based POMOFs with different nuclear cobalt clusters for photoreduction of CO_2 to produce syngas. J Mater Chem C, 2023, 11: 7389–7396

37 Zhuo TC, Song Y, Zhuang GL, *et al.* H-bond-mediated selectivity control of formate *versus* CO during CO_2 photoreduction with two cooperative Cu/X sites. J Am Chem Soc, 2021, 143: 6114–6122

38 Kou J, Wu Q, Cui D, *et al.* Selective encapsulation and chiral induction of C_{60} and C_{70} fullerenes by axially chiral porous aromatic cages. Angew Chem Int Ed, 2023, 62: e202312733

39 Saha S, Das G, Thote J, *et al.* Photocatalytic metal-organic framework from CdS quantum dot incubated luminescent metallohydrogel. J Am Chem Soc, 2014, 136: 14845–14851

40 Dong M, Zhou J, Zhong J, *et al.* CO_2 dominated bifunctional catalytic

sites for efficient industrial exhaust conversion. Adv Funct Mater, 2022, 32: 2110136

41 Wang JW, Qiao LZ, Nie HD, *et al*. Facile electron delivery from graphene template to ultrathin metal-organic layers for boosting CO_2 photoreduction. Nat Commun, 2021, 12: 813

42 Guo S, Kong L-, Wang P, *et al*. Switching excited state distribution of metal-organic framework for dramatically boosting photocatalysis. Angew Chem Int Ed, 2022, 61: e202206193

43 Yan ZH, Du MH, Liu J, *et al*. Photo-generated dinuclear {Eu(II)}2 active sites for selective CO_2 reduction in a photosensitizing metal-organic framework. Nat Commun, 2018, 9: 3353

44 Yin HQ, Zhang ZM, Lu TB. Ordered integration and heterogenization of catalysts and photosensitizers in metal-/covalent-organic frameworks for boosting CO_2 photoreduction. Acc Chem Res, 2023, 56: 2676–2687

45 Fu S, Yao S, Guo S, *et al*. Feeding carbonylation with CO_2 *via* the synergy of single-site/nanocluster catalysts in a photosensitizing MOF. J Am Chem Soc, 2021, 143: 20792–20801

46 Guo SH, Qi XJ, Zhou HM, *et al*. A bimetallic-MOF catalyst for efficient CO_2 photoreduction from simulated flue gas to value-added formate. J Mater Chem A, 2020, 8: 11712–11718

Author contributions   Gu J and Han X designed the experiments, wrote the original draft, participated in the design and layout of the pictures and reviewed the manuscript. Sun C, Shan G and Su Z conceived the idea, supervised the work, and reviewed and revised the manuscript. He D, and Zhou F supervised the work. He J, You S and Dong M helped with the characterization test.

Conflict of interest   The authors declare that they have no conflict of interest.

Supplementary information   Experimental details and supporting data are available in the online version of the paper.
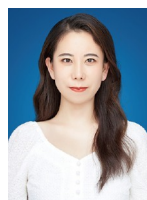
Jianxia Gu obtained her PhD from Northeast Normal University under the supervision of Prof. Chunyi Sun and Prof. Xinlong Wang in 2021. She is currently working at Xinzhou Teachers University. Her research is mainly related to the development of MOF-based and POM-based materials applied in the fields of photocatalysis and electrocatalysis.

Chunyi Sun received her PhD degree in 2015 under the supervision of Prof. Zhongmin Su from Northeast Normal University. She studied at the University of Hong Kong as an exchang student during her PhD studies under the supervision of Prof. Chi-Ming Che. She worked as a research assistant in Prof. Chi-Ming Che's group in the Hong Kong University from 2016 to 2017. She has been an associate professor and doctor supervisor in Northeast Normal University since 2019. And she is now a professor at the School of Chemistry, Northeast Normal University. Her main research interest is mainly related to the photoelectrochemical catalysis with crystalline porous materials as catalysts.

二维金属偶氮盐框架用于高效二氧化碳光还原

谷建霞[1,3], 王龄欣[4], 韩旭[2,4*], 贺敬婷[4], 由思琦[3], 董曼[3], 单国刚[3*], 何丹凤[2], 周付江[2], 孙春义[3*], 苏忠民[4]

摘要   由可见光驱动的将CO_2转化为高附加值燃料是一种清洁可再生的技术, 有助于控制全球变暖和应对能源短缺. 近年来, 二维的金属偶氮盐框架(2D MAFs)因其特定的电子传输路径、高度暴露的表面活性位点及可调节的吸光能力, 在CO_2光还原研究中备受关注. 然而, 对其在该领域的研究仍处于初级阶段. 本文设计了一种新型二维MAFs (compound 1), 通过四-(4-四唑基苯基)乙烯(H4TTPE)与钴的自组装实现了对CO_2的光还原. 作为对比, 通过类似的合成过程构建了具有三维结构的compound 2. 非均相光催化实验结果显示, 2D compound 1的光还原性能明显优于3D compound 2, 在相同条件下, 其CO产率高达11.56 mmol g^{-1} h^{-1}, 是compound 2 (1.94 mmol g^{-1} h^{-1})的6倍. 这一性能优势源于compound 1独特的二维结构, 其不仅具有有利于CO_2还原的能级, 还能在整个CO_2光还原过程中促进电子-空穴高效分离. 本工作作为设计适用于高效CO_2光还原的2D MAFs光催化剂指引了方向.